



# Cobalt-doped basic iron phosphate as bifunctional electrocatalyst for long-life and high-power-density rechargeable zinc-air batteries

Lutao Song<sup>a,1</sup>, Tianlong Zheng<sup>b,1</sup>, Lirong Zheng<sup>c</sup>, Bin Lu<sup>a,\*</sup>, Hengquan Chen<sup>b</sup>, Qinggang He<sup>b,\*</sup>, Wanzhen Zheng<sup>b</sup>, Yang Hou<sup>b</sup>, Jiale Lian<sup>a</sup>, Yang Wu<sup>a</sup>, Jian Chen<sup>d</sup>, Zhizhen Ye<sup>a,e</sup>, Jianguo Lu<sup>a,e,\*\*</sup>

<sup>a</sup> State Key Laboratory of Silicon Materials, Key Laboratory for Biomedical Engineering of Ministry of Education, School of Materials Science and Engineering, Zhejiang University, Hangzhou 310027, PR China

<sup>b</sup> College of Chemical and Biological Engineering, Zhejiang University, Hangzhou 310027, PR China

<sup>c</sup> Institute of High Energy Physics, Chinese Academy of Sciences (CAS), Beijing 100049, PR China

<sup>d</sup> State Key Laboratory of Fluid Power & Mechatronic Systems, School of Mechanical Engineering, Zhejiang University, Hangzhou 310027, PR China

<sup>e</sup> Wenzhou Institute, Zhejiang University, Wenzhou 325036, PR China

## ARTICLE INFO

### Keywords:

Cobalt-doped basic iron phosphate  
Bifunctional electrocatalyst  
Oxygen reduction reaction  
Oxygen evolution reaction  
Rechargeable Zn-air battery  
Water-oil two-phase hydrothermal method

## ABSTRACT

High-efficient and long-cycle air cathodes are crucial for the development of rechargeable zinc-air batteries (ZABs). Herein, we develop a strategy of micro-spherical cobalt-doped  $\text{Fe}_5(\text{PO}_4)_4(\text{OH})_3 \cdot \text{H}_2\text{O}$  (Co-FPOH), synthesized by a novel water-oil two-phase hydrothermal method, which was used as ORR/OER bifunctional electrocatalyst for ZABs. The change of local electronic distribution is identified by doping of Co into  $\text{Fe}_5(\text{PO}_4)_4(\text{OH})_3 \cdot \text{H}_2\text{O}$  (FPOH), effectively improving the electrocatalytic performance of the resulted Co-FPOH. The OER overpotential of Co-FPOH (290 mV) far outperforms state-of-the-art  $\text{RuO}_2$  (350 mV); the ORR catalytic reaction of Co-FPOH is near  $4e^-$ , almost reaching the theoretical value of Pt/C ( $n = 4.00$ ). The ZAB assembled with Co-FPOH as an air electrode exhibits an ultralong cycling lifetime of 450 h at  $5 \text{ mA cm}^{-2}$ , a super high peak power density of  $167.8 \text{ Wh cm}^{-2}$ , a high open circuit voltage of about 1.42 V and a large discharge specific capacity of  $817 \text{ mAh g}_{\text{Zn}}^{-1}$  at  $10 \text{ mA cm}^{-2}$ . The proposed Co-FPOH is expected to outperform precious metal electrocatalysts as a potential bifunctional electrocatalyst for advanced ZABs. Also, this work offers a novel strategy to synthesize excellent bifunctional electrocatalysts for this kind of energy-related electrocatalytic reactions.

## 1. Introduction

Developing sustainable clean energy storage and conversion technology is a significant challenge to achieve low-carbon emission and promote the steady growth of global economy [1–10]. Among various energy storage devices, rechargeable zinc-air batteries (ZABs) are considered as the very important one, owing to their high theoretical energy density ( $1084 \text{ Wh kg}^{-1}$ ), non-toxicity, low cost, and environmentally benign [11–13]. However, the large overpotential of reactions on air cathode during cycling seriously hinder the practical application of ZABs [14]. Oxygen reduction reaction (ORR) and oxygen evolution

reaction (OER) are chief reactions occurring in the air cathode of ZABs [15,16]. It is well known that the sluggish reaction kinetics is caused by the two catalytic reactions of four electron transfer process, which needs to overcome a considerable energy barrier [17–19]. To solve these issues, researchers have invested a lot of efforts to explore high-performance bifunctional electrocatalysts. So far,  $\text{RuO}_2$  and  $\text{IrO}_2$  have been considered as the most active materials for OER, and Pt/C are the best candidate for ORR, which have been both investigated in depth [20]. Unfortunately, the large-scale application in ZABs has been restricted by their high production cost, low element content, and poor long-cycle stability [21–23]. Hence, it is urgent to elaborately design

\* Corresponding authors.

\*\* Corresponding author at: State Key Laboratory of Silicon Materials, Key Laboratory for Biomedical Engineering of Ministry of Education, School of Materials Science and Engineering, Zhejiang University, Hangzhou 310027, PR China.

E-mail addresses: [binlu@zju.edu.cn](mailto:binlu@zju.edu.cn) (B. Lu), [qghe@zju.edu.cn](mailto:qghe@zju.edu.cn) (Q. He), [lujianguo@zju.edu.cn](mailto:lujianguo@zju.edu.cn) (J. Lu).

<sup>1</sup> These authors contributed equally to this work

bifunctional non-noble metal-based electrocatalysts with low cost and long-term cycle stability for advanced ZABs.

As a replacement for a class of precious metal-based catalysts, transition metal materials, such as transition metal oxides [24,25], hydroxides [26], sulfides [27–32], selenides [33,34], carbides [35], borides [36], phosphides [37], nitrides [38,39], phosphates [40,41], and others [42], have aroused intensively interest. Particularly, transition metal phosphates, such as Fe-Pi, Co-Pi, and Ni-Pi, are regarded as a class of low cost and environmentally friendly electrocatalysts [43,44]. Also, TMPi with different coordination modes can stabilize metal centers with catalytic activity [45]. Transition metal atoms (such as Fe and Co) have small 3d orbitals and lower crystal field activation energy, contributing to the electrocatalytic ORR/OER process. Doping other transition metal ions (such as Mn [46] and Ni [47]) into transition metal phosphate has been proved to enhance the electrocatalytic behaviors by changing local electronic structure and the number of active sites because of the synergistic effect between the metallic ions. Li et al. [48] lately indicated that the substitute of Ni atom by Fe atom in Ni-Pi, forming Ni:Pi-Fe, could transform the electronic structure and strengthen the synergistic effect of iron and nickel that significantly increased the OER performance. Sultan et al. [49] also demonstrated that bimetallic  $\text{Fe}_3\text{Co}(\text{PO}_4)_4$  nanoparticles (NPs) homogeneously distributed on the rGO surface had excellent electrocatalytic activity toward OER in alkaline media. However, transition metal phosphates are rarely reported as ORR/OER bifunctional electrocatalysts and an advanced air cathode for ZABs at present [50].

In this work, we elaborately design a novel micro-spherical  $\text{Fe}_5(\text{PO}_4)_4(\text{OH})_3 \cdot \text{H}_2\text{O}$  (FPOH) and cobalt-doped  $\text{Fe}_5(\text{PO}_4)_4(\text{OH})_3 \cdot \text{H}_2\text{O}$  (Co-FPOH) by a water-oil two-phase hydrothermal method for the first time. The as-prepared Co-FPOH demonstrates excellent electrocatalysis performance in ORR/OER and can therefore be used as cathode material for advanced ZABs. The resulted Co-FPOH reveals fairly high OER activity with an overpotential of merely 290 mV at a current density of 10  $\text{mA cm}^{-2}$ . The air electrode made from Co-FPOH exhibits superior electrochemical performance of ZABs, having a stable open circuit voltage of about 1.42 V, a large discharge specific capacity of 817  $\text{mAh g}_{\text{Zn}}^{-1}$  at 10  $\text{mA cm}^{-2}$ , an ultralong cycling lifetime of 450 h at 5  $\text{mA cm}^{-2}$  and a super high peak power density of 167.8  $\text{Wh cm}^{-2}$ . Our study offers a novel strategy to synthesize potential bifunctional ORR/OER electrocatalysts for advanced ZABs.

## 2. Experimental

### 2.1. Materials and reagents

Cobalt stearate and iron stearate were supplied by Shanghai Dibo Biological Technology Co., Ltd. Toluene, phytic acid (50 wt% in water), potassium hydroxide, zinc acetate tetrahydrate, ruthenium dioxide and platinum/carbon (20 wt%) were bought from Macklin. Nafion solution (5 wt%) for catalyst slurry and carbon paper supported on nickel mesh required for air cathode were provided by Hesen Electric Co., Ltd. In this experiment, the chemical reagents purchased from the company are used directly without further purification.

### 2.2. Synthesis of electrocatalysts

FPOH was synthesized by a facile water-oil two-phase hydrothermal method. Typically, a pipette was used to take 0.6 mL of phytic acid and the solution A was formed by dissolving it in 40 mL deionized water. Next, 2 mmol of  $\text{Fe}(\text{C}_{17}\text{H}_{35}\text{COO})_3$  was weighed into a centrifuge tube containing 40 mL of toluene and the centrifuge tube was sonicated about 4 h to uniformly disperse the  $\text{Fe}(\text{C}_{17}\text{H}_{35}\text{COO})_3$  in toluene to form a solution B. Eventually, solution A and solution B were poured into 100 mL Teflon-linked stainless steel autoclave in order and stored in an oven at 180 °C for one day. The light green precipitate was treated by centrifugation and washing 3–4 times with deionized water and ethanol,

followed by drying at 60 °C for about 12 h. The Co-FPOH electrocatalyst had similar synthesis procedures as above, with that only 2 mmol of  $\text{Fe}(\text{C}_{17}\text{H}_{35}\text{COO})_3$  was replaced with 0.4 mmol of  $\text{Fe}(\text{C}_{17}\text{H}_{35}\text{COO})_3$  and 1.6 mmol of  $\text{Co}(\text{C}_{17}\text{H}_{35}\text{COO})_2$ .

### 2.3. Material characterization

The crystal structure of the synthesized FPOH and Co-FPOH was analyzed by Rigaku D/max RA X-ray diffractometer (XRD). The micro morphology and element distribution of as-synthesized materials were observed by Hitachi S-400 scanning electron microscope (SEM) and FEI Tecnai G2 F30 transmission electron microscope (TEM). The surface chemical elements analysis was implemented by using an X-ray photoelectron spectroscopy (XPS) in an AXIS Supra system. The chemical groups of materials were detected by NICOTCT Fourier infrared spectroscopy (FT-IR) and Senterra confocal laser micro Raman spectroscopy. The valence of the material and the coordination relationship between metal atoms (Fe, Co) were detected by X-ray absorption spectroscopy (XAS) at Beijing Synchrotron Radiation Facility.

### 2.4. Electrochemical measurements

CHI760E (Chenhua Instrument Co., Ltd., Shanghai) electrochemical workstation equipped with rotating disk/ring electrode (RDE/RRDE Yinhe, Taizhou) was used to conduct all of the electrocatalytic measurements at 25 °C. Hg/HgO electrode was used as the reference electrode and graphite rod was used as the counter electrode. In this experiment, the working electrodes are RDE (area: 0.1257  $\text{cm}^2$ ) and RRDE (area: 0.1866  $\text{cm}^2$ ). For preparing the working electrode, 10 mg catalyst sample and 10 mg Ketjen Black were dispersed in a mixed solution (40 mL isopropanol and 80  $\mu\text{L}$  Nafion), following 40 min of sonication to form a well dispersed catalyst slurry. After then, catalyst slurry was dropped on the working electrode with a pipette and dried for several hours at 25 °C for later use. The mass density of the catalyst loading is 0.283  $\text{mg cm}^{-2}$ . The potential obtained in the experiment is converted into reversible hydrogen electrode (RHE) by Nernst equation:

$$E_{\text{RHE}} = E_{\text{Hg/HgO}} + 0.0591 \times \text{pH} + 0.098 \quad (1)$$

where  $E_{\text{RHE}}$  is the reversible hydrogen electrode potential value,  $E_{\text{Hg/HgO}}$  is the potential directly obtained on the instrument, and the pH value is 14 for OER and 13 for ORR.

All electrocatalytic tests were carried out in pure oxygen/nitrogen saturated KOH solution (0.1 M for ORR and 1.0 M for OER). The electrocatalytic polarization curves obtained by linear sweep voltammetry (LSV) were carried out at a scan rate of 10  $\text{mV s}^{-1}$ . The electrochemical impedance spectroscopy (EIS) was performed at 1.56 V at a frequency of 100,000–0.1 Hz for OER. The double-layer capacitance ( $C_{\text{dl}}$ ) was calculated by cyclic voltammetry (CV) at different scan rates (20, 40, 60, 80, 100  $\text{mV s}^{-1}$ ). The oxygen reduction stability of Co-FPOH and Pt/C was tested at 0.5 V (vs. RHE). The LSV tests were performed with 90% IR compensated, similar to those previously reported such as Ref. [51]. The LSV polarization curve of ORR was conducted at 400, 900, 1200, 1600, 2000, and 2500 rpm with saturated pure  $\text{O}_2$ . From RDE test, the electron transfer number ( $n$ ) was computed by Koutechy–Levich (K–L) equation:

$$1/J = 1/J_k + 1/B\omega^{1/2} \quad (2)$$

$$B = 0.2nFC_0(D_0)^{2/3}\nu^{-1/6} \quad (3)$$

where  $J$  is the experimentally acquired current density ( $\text{mA cm}^{-2}$ ),  $J_k$  is the kinetic current ( $\text{mA cm}^{-2}$ ),  $n$  is the number of electrons transferred,  $\omega$  is the electrode rotating rate (rpm),  $F$  is the Faraday constant (96,485  $\text{C mol}^{-1}$ ),  $C_0$  is the concentration of oxygen (0.0012  $\text{mol L}^{-1}$ ),  $D_0$  is the diffusion coefficient of oxygen molecules ( $1.9 \times 10^{-5} \text{ cm}^2 \text{ s}^{-1}$ ), and  $\nu$  is the kinematics viscosity (0.01  $\text{cm}^2 \text{ s}^{-1}$ ). As can be seen from Eq. (2), with  $J^{-1}$  as the ordinate and  $\omega^{-1/2}$  as the abscissa, the slope of the

fitting line can be obtained through linear fitting and slope =  $B^{-1}$ . After then,  $n$  value can be calculated by Eq. (3). The yield of hydrogen peroxide ( $\%H_2O_2$ ) and corresponding  $n$  value can be calculated according to the following formulas (4) and (5).

$$\%H_2O_2 = \frac{200I_R/N}{I_D+I_R/N} \quad (4)$$

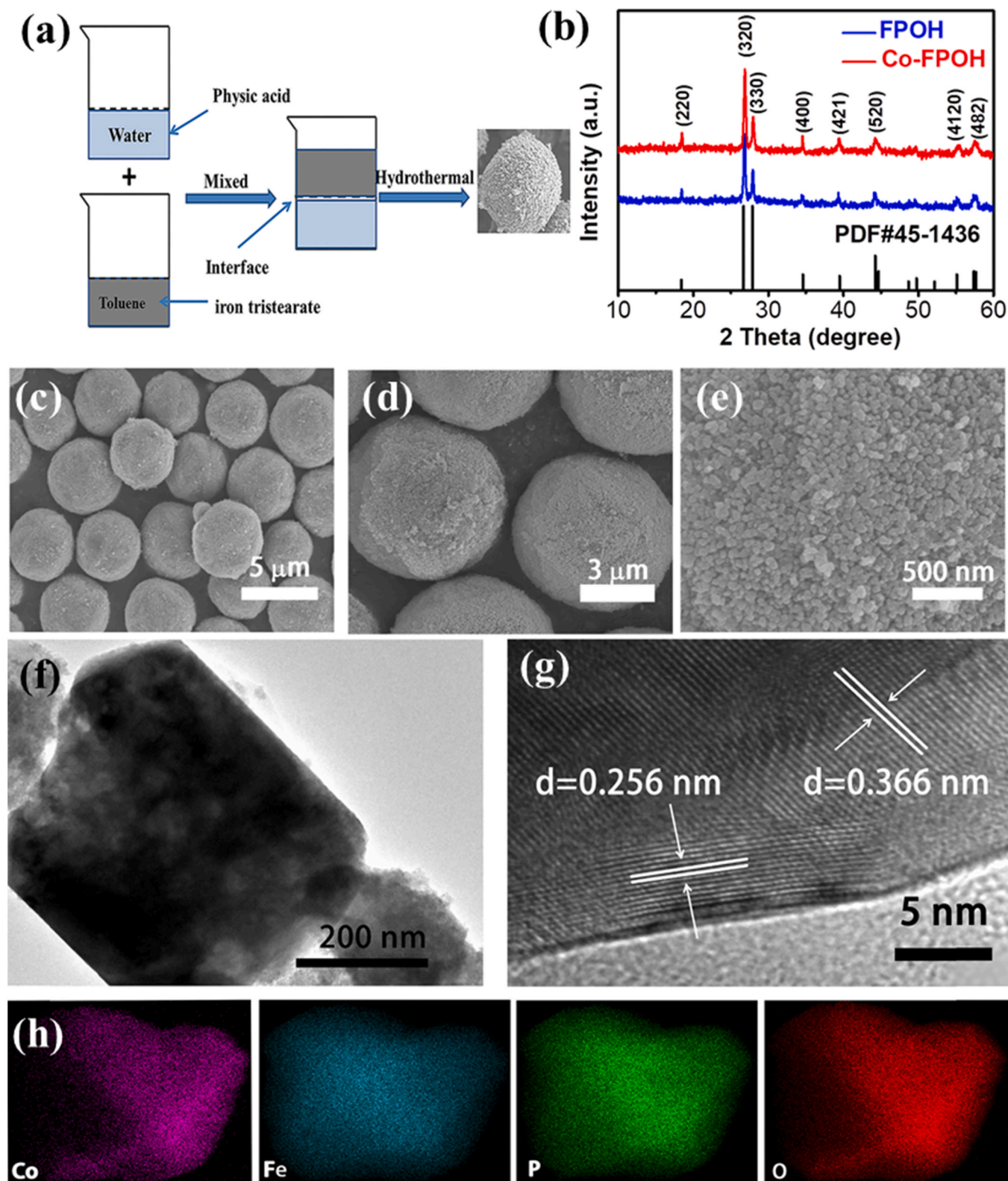


**Fig. 1.** (a) Schematic illustration of the synthesis of microspherical FPOH and Co-FPOH; (b) XRD patterns of Co-FPOH and FPOH; (c–e) SEM images with different magnifications for Co-FPOH; (f, g) TEM and HRTEM images of Co-FPOH. (h) EDX elemental mapping of Co-FPOH.



$$n = \frac{4I_D}{I_D + \frac{I_R}{N}} \quad (5)$$

where %H<sub>2</sub>O<sub>2</sub> is the yield of hydrogen peroxide,  $I_R$  is the current of ring,  $I_D$  is the current of disk, and  $N$  is a constant (0.37).

## 2.5. Aqueous zinc-air batteries

The ZAB was assembled by a polished zinc, carbon paper supported active material, and electrolyte (6 M KOH and 0.2 M Zn(CH<sub>3</sub>COO)<sub>2</sub>). The loading amount of active material on carbon paper is 1 mg cm<sup>-2</sup>. The galvanostatic discharge curves were recorded with CHI 760E workstation and the corresponding power density was derived from the measured data. The charge/discharge curve, specific capacity, open-circuit voltage curves and rate performance were measured on a CT2001 A LANHE test instrument.

## 3. Results and discussion

### 3.1. Material synthesis and characterization

The synthetic illustration of Co-FPOH electrocatalyst is depicted in Fig. 1a. The micro-spherical Co-FPOH was acquired by a facile water-oil two-phase hydrothermal method using iron stearate, cobalt stearate and phytic acid [52]. Crystal structures of samples were initially investigated by powder XRD analysis, and the obtained images are shown in Fig. 1b.

The as-prepared FPOH microspheres show typical diffraction peaks, matching well with the standard data of the giniite Fe<sub>5</sub>(PO<sub>4</sub>)<sub>4</sub>(OH)<sub>3</sub>·H<sub>2</sub>O (JCPDS No. 45-1436). After cobalt doping, the pattern of the Co-FPOH shows no obvious changes compared with that of FPOH microspheres, suggesting no extra new phase generation.

The SEM images of Co-FPOH (Fig. 1c and Fig. 1d) and FPOH (Fig. S1) illustrate 3D microspheres with a rough surface, having an average size of 3–5 μm. As shown in Fig. 1e, each microsphere is formed by agglomeration of many small nanoparticles. The EDS image (Fig. S2) demonstrates Co-FPOH electrocatalyst comprised of Fe, Co, and P as well as O elements, which also verifies an about 1/4 = Co/Fe atomic ratio, suggesting the cobalt was successfully doped into the as-synthesized FPOH. The microstructure of Co-FPOH is further investigated by high-resolution TEM. The TEM image showed in Fig. 1f was from the surface of a microsphere, where the microscopic morphology of the block is consistent with that in the SEM image. The crystal lattice fringe distance of 0.256 and 0.366 nm corresponds to the (400) and (320) planes of Co-FPOH, respectively (Fig. 1g). The EDS element mapping of Co-FPOH (Fig. 1h) displays the homogeneous distribution of Co, Fe, P and O. All the above results demonstrate that Co-FPOH is formed, which is of significance to accelerate ORR/OER process.

The Raman and FTIR spectra were applied to investigate the chemical composition of samples. As shown in Fig. 2a, the sharp band at 878, 990, and 1105 cm<sup>-1</sup> can be described as symmetric PO<sub>4</sub><sup>3-</sup> stretching vibration of samples [53]. We can get similar conclusions from FT-IR spectra (Fig. 2b) as well. The bands in the range of 400–700 cm<sup>-1</sup> are

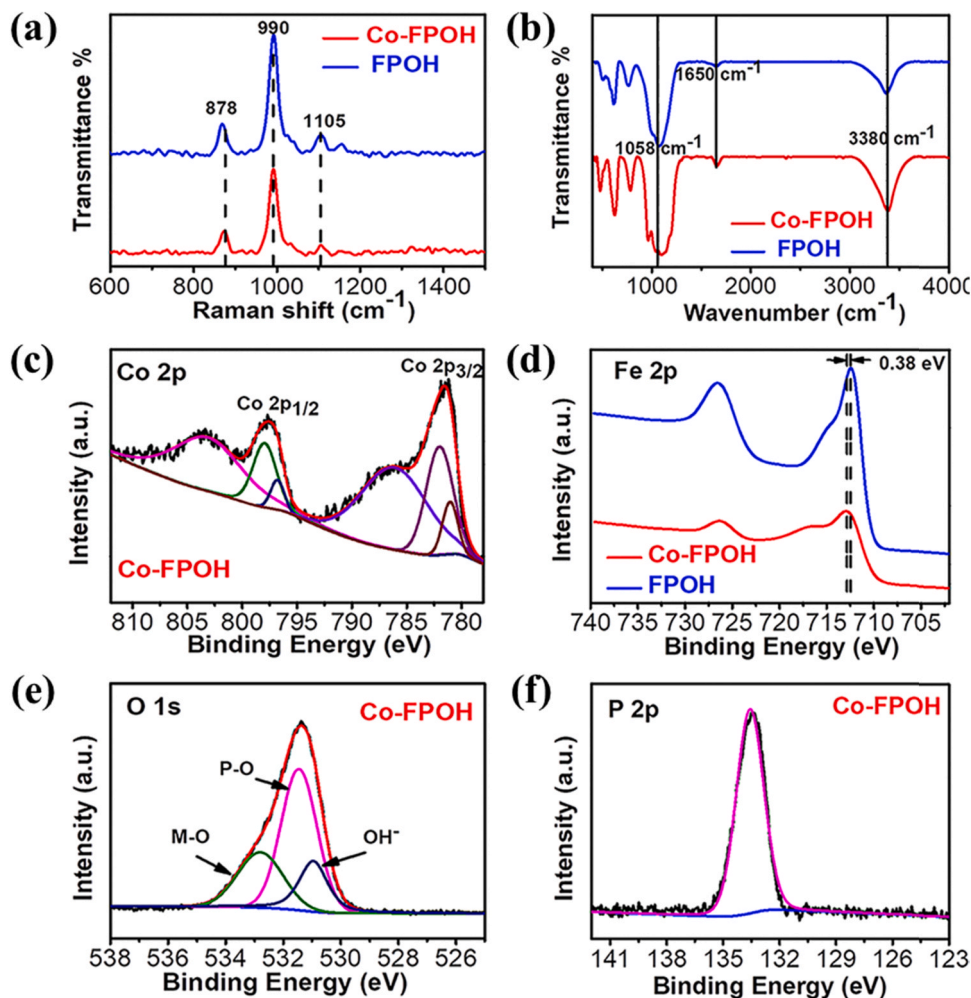


**Fig. 2.** (a) Raman spectra, and (b) FT-IR spectra of FPOH and Co-FPOH; (c) XPS spectra of Co 2p of Co-FPOH; (d) XPS spectra of Fe 2p of Co-FPOH and FPOH. High-resolution (e) O 1s, and (f) P 2p of Co-FPOH.

derived from metal-oxygen stretching vibration [54]. Like in every kind of hydroxide compound, water molecules of physical surface adsorption and hydroxyl groups can be clearly probed around  $3400\text{ cm}^{-1}$  [43]. The band centered at  $1058$  and  $1650\text{ cm}^{-1}$  is described as stretching vibration of P-O and hydroxyl in compounds, respectively [55,56].

The surface chemical states were investigated by the typical scan XPS for the as-prepared samples. The XPS overall spectra of Co-FPOH demonstrate the existence of Co, Fe, P and O in the as-synthesized sample (Fig. S3a), which is following the above EDS result. In the FPOH, the presence of Fe, P, and O is also detected by the XPS survey spectra (Fig. S3b). As exhibited in Fig. 2c, the high resolution Co 2p spectra contain two main peaks at binding energy (BE) of  $797.95$  and  $782.00\text{ eV}$ , with two broad satellite peaks at  $803.13$  and  $786.08\text{ eV}$ , demonstrating the presence of Co (II) phase [11,41,57]. Besides, the other two relative weak peaks at  $796.78$  and  $781.04\text{ eV}$  suggest the presence of a high oxidation state of the Co (III) phase [58]. Fe 2p spectra of Co-FPOH and FPOH is given in Fig. 2d, where the two peaks at  $712.81$  and  $726.14\text{ eV}$  are attributed to Fe  $2p_{3/2}$  and  $2p_{1/2}$ , which demonstrates the presence of Fe (III) in the as-prepared material [41, 50]. After cobalt doping, the Fe 2p curve shifts to higher binding energy at a value of about  $0.38\text{ eV}$ , suggesting the interaction between cobalt and iron [58], which also reveals the change of chemical environment of Fe in FPOH by the Co doping. As displayed in Fig. 2e, the O 1s spectrum of the Co-FPOH exhibits three peaks at  $530.95$ ,  $531.45$ , and  $532.79\text{ eV}$ . The peak at  $530.95\text{ eV}$  is attributed to the typical chemical bond of metal-oxygen. A sharp peak around  $531.45\text{ eV}$  is indexed to the presence of the phosphate group. Besides, the peak  $\sim 532.79\text{ eV}$  is due to the existence of the OH [48,59]. In Fig. 2f, the sharp peak at around  $133.56\text{ eV}$  in P 2p spectrum suggests the presence the metal-phosphate [59].

To obtain other information of the chemical state and element coordination chemical environment of Co and Fe atoms in as-prepared Co-FPOH and FPOH electrocatalyst, X-ray absorption near edge structure (XANES) and Fourier transform-extended X-ray absorption fine structure (FT-EXAFS) spectra were investigated. Fig. 3a shows the Co K-edge

XANES profiles, demonstrating the oxidation state of doped Co atoms in Co-FPOH located at higher than Co(II)O and lower than  $\text{Co}_2(\text{III})\text{O}_3$ , suggesting the average valence state of doped Co is between  $+2$  and  $+3$ . This result is consistent with the high resolution Co 2p XPS spectra [60]. The Fe K-edge XANES curves in Fig. 3b demonstrates the adsorption edges do not have any noticeable change. However, the intensity of the white line around  $7130\text{ eV}$  increases after cobalt doping [60]. The white line corresponds to the dipole allowed  $1s \rightarrow 4p$  transition, and it is related to the oxidation valence state and the distance between atoms. Hence, the change of the intensity of the white line indicates a small part of Fe atoms in Co-FPOH may enter into a higher oxidation state [60,61].

As exhibited in Fig S4 and Table S1, the two characteristic peaks at  $1.1$  and  $1.2\text{ \AA}$  are formed by two Fe-O scattering paths with different atomic distances. And the characteristic peaks at  $2.5$  and  $2.8\text{ \AA}$  correspond to Fe-Fe and Fe-P, respectively [61,62]. As shown in Fig. 3c, the FT-EXAFS curve of Fe K-edge in Co-FPOH only reveals a Fe-O single scattering characteristic peak. The fitting results show that the atomic distance of Fe-O in Co-FPOH is between Fe-O1 and Fe-O2 in FPOH, indicating the atomic distance between Fe-O tends to average after Co doping [62]. It is worth mentioning that the Fe K-edge in Co-FPOH is not easy to analyze, due to the K absorption edge energies of Fe and Co are similar. As shown in Fig. 3d, the characteristic peak at  $1.6\text{ \AA}$  in Co K-edge corresponds to a single scattering between Co-O nearest to the first shell. The subsequent characteristic peaks are attributed to the scattering of Co-M ( $M = \text{Fe, Co}$ ) and Co-P, indicating Co is successfully doped into FPOH [60,63]. These results advantageously prove that the chemical environment or electronic structure around the Fe atom has changed. The change of local electronic distribution by doping of Co into FPOH, as identified here, is believed to be responsible for improving electrocatalytic performance of the resulted Co-FPOH.

### 3.2. The OER performance of FPOH and Co-FPOH electrocatalyst

The OER performance significantly affects ZABs due to the sluggish reaction kinetics of four electron transfer during the charging process.

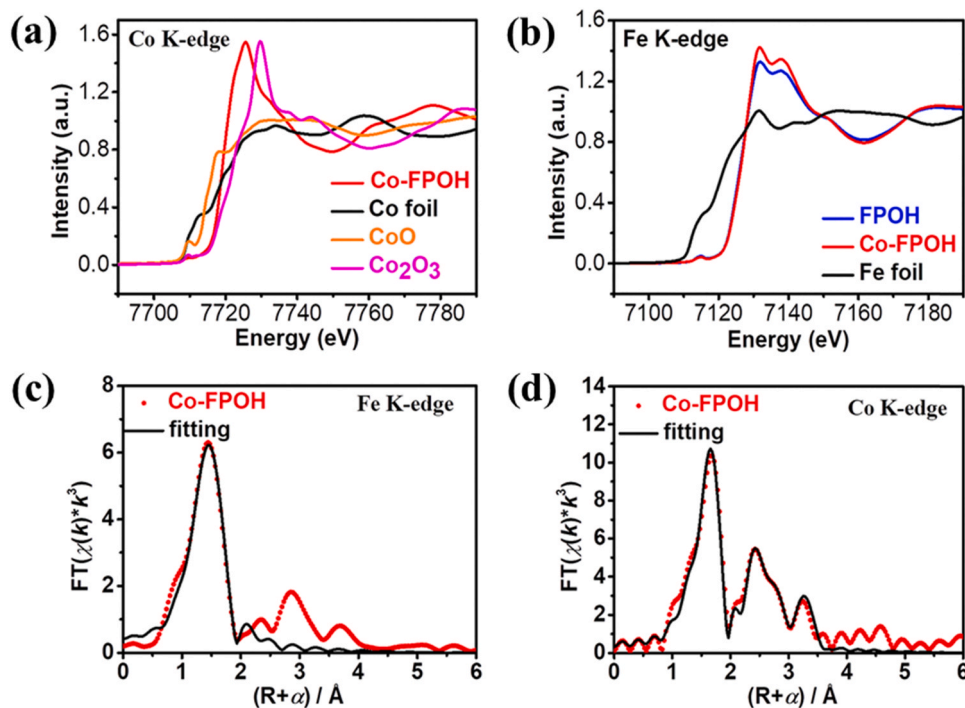


**Fig. 3.** XANES spectra of Co-FPOH and reference materials (a) Co K-edge, and (b) Fe K-edge; (c) Fe K-edge EXAFS (points) and curve fitted (line) for Co-FPOH, shown in R-space (FT-magnitude); (d) Co K-edge EXAFS (points) and curve fitted (line) for Co-FPOH, shown in R-space (FT-magnitude). The data is  $k^3$ -weighted and not phase-corrected.

[64]. The LSV curves of three catalysts are shown in Fig. 4a. The Co-FPOH achieved the lowest overpotential (290 mV) at  $10 \text{ mA cm}^{-2}$  among the counterparts, namely FPOH (330 mV), and  $\text{RuO}_2$  (350 mV). Besides, the OER overpotential of Co-FPOH is lower than those of presently reported catalysts (Table S2). The Tafel slope is derived from Tafel formula to clarify the OER kinetic process of three electrocatalysts [65]. As shown in Fig. 4b, the Tafel slope of Co-FPOH ( $69 \text{ mV dec}^{-1}$ ) is much lower than those of  $\text{RuO}_2$  ( $107 \text{ mV dec}^{-1}$ ) and FPOH ( $175 \text{ mV dec}^{-1}$ ), respectively. Therefore, Co-FPOH has higher catalytic performance than FPOH and  $\text{RuO}_2$  in OER. Meanwhile, the features of Co-FPOH and FPOH have such a vast difference, which may mean that the doping of Co atoms changes the local electronic distribution [58].

To demonstrate the origin of electrocatalytic activity, double-layer capacitance ( $C_{dl}$ ) and EIS curves were evaluated. CV curves in 0.624 – 1.024 V were adopted to compute the  $C_{dl}$ . Six CV curves were acquired from six different scan rates. Fig. 4c displays the CV curve of Co-FPOH and other catalysts are shown in Fig. S5. As demonstrated in Fig. 4d, the Co-FPOH achieves the highest  $C_{dl}$  ( $45.12 \text{ mF cm}^{-2}$ ), obviously higher than that of FPOH ( $35.23 \text{ mF cm}^{-2}$ ) and commercial  $\text{RuO}_2$  ( $30.17 \text{ mF cm}^{-2}$ ), which demonstrates the doping of cobalt atoms significantly improve the  $C_{dl}$  with enormous electrochemical active reactive sites for OER process [66]. Then, the EIS was carried out to investigate the interfacial kinetics of as-prepared samples. From Nyquist curves, charge transfer resistance ( $R_{ct}$ ) at the interface between the electrolyte and the electrode is deduced from the intercept of the

semicircle in the high-frequency region [48]. Fig. 4e demonstrates that all the catalysts have similar solution resistance ( $R_s$ ). Furthermore, all values of  $R_{ct}$  and  $R_s$  are listed in Table S3. The Co-FPOH exhibits the lowest  $R_{ct}$  ( $26.11 \Omega$ ), indicating most excellent reaction kinetics in keeping with LSV polarization data and Tafel slopes. As a key index, the durability of as-prepared Co-FPOH was conducted by a continuous CV scanning test to evaluate the practical application of electrocatalyst. As illustrated in Fig. 4f, the LSV polarization curves of Co-FPOH remain nearly overlapped to the prior after 500 cycling test, indicating its excellent durability during the OER process.

### 3.3. The ORR performance of FPOH and Co-FPOH electrocatalyst

The ORR performance is also significantly important for the bifunctional electrocatalytic electrode, especially for that used in ZABs. The electrocatalytic activity of ORR was investigated in oxygen-saturated electrolyte by RDE/RRDE. As demonstrated in Fig. 5a, the Co-FPOH exhibits relatively excellent electrocatalytic activity with an onset potential ( $E_{onset}$ ) of 0.82 V and a half-wave potential ( $E_{1/2}$ ) of 0.69 V, evidently higher than those of FPOH ( $E_{onset} = 0.71 \text{ V}$ ,  $E_{1/2} = 0.60 \text{ V}$ ), indicating that Co-FPOH has more superior ORR electrocatalytic activity than FPOH. Although the  $E_{onset}$  and  $E_{1/2}$  of Co-FPOH are lower than those of commercial Pt/C ( $E_{onset} = 1.0 \text{ V}$ ,  $E_{1/2} = 0.85 \text{ V}$ ), it is still acceptable values for practical applications, especially for an ORR/OER bifunctional electrocatalyst. More information

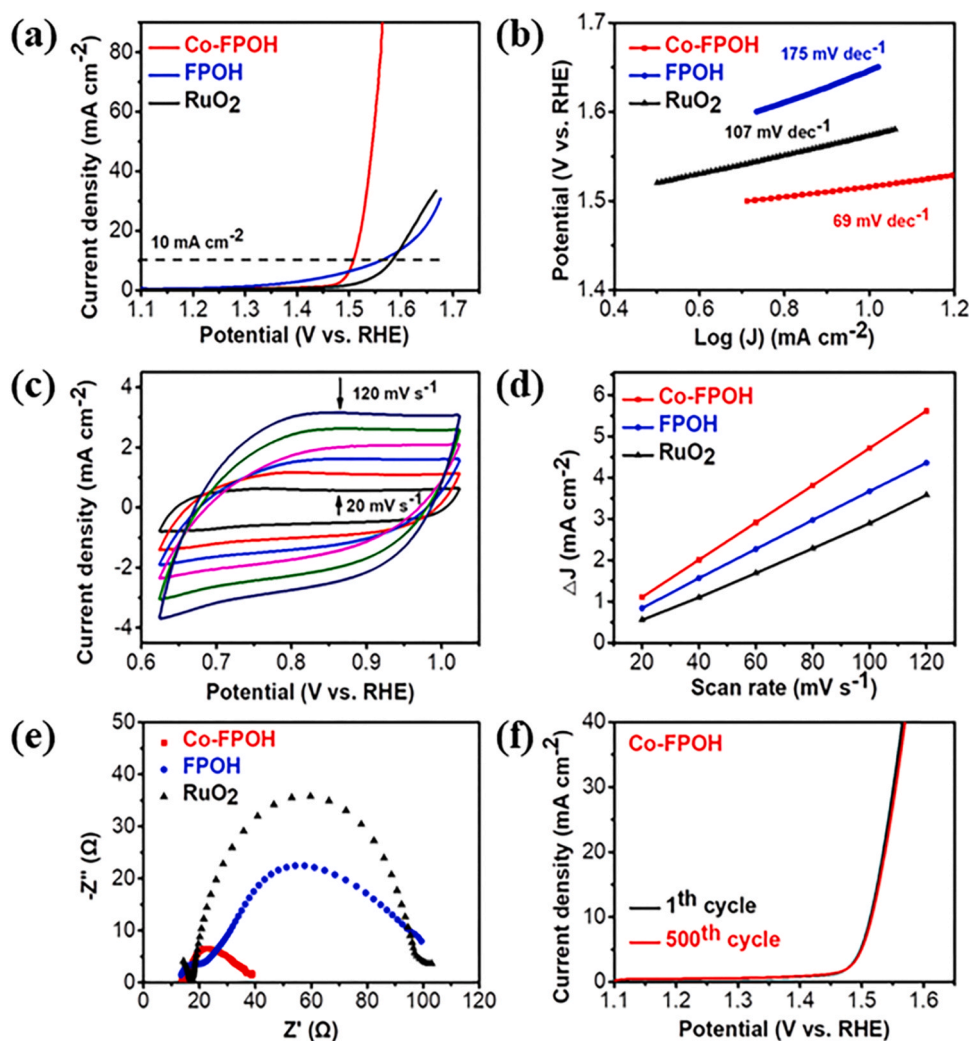


**Fig. 4.** OER electrocatalytic activity of Co-FPOH, FPOH and benchmark  $\text{RuO}_2$  in 1.0 M KOH (a) LSV curves, and (b) Tafel slopes; (c) CVs scanning of Co-FPOH with a different rate of 20–120  $\text{mV s}^{-1}$ ; (d) Double-layer capacity ( $C_{dl}$ ), and (e) Nyquist plots of Co-FPOH, FPOH and benchmark  $\text{RuO}_2$ ; (f) Cyclic aging test of Co-FPOH.



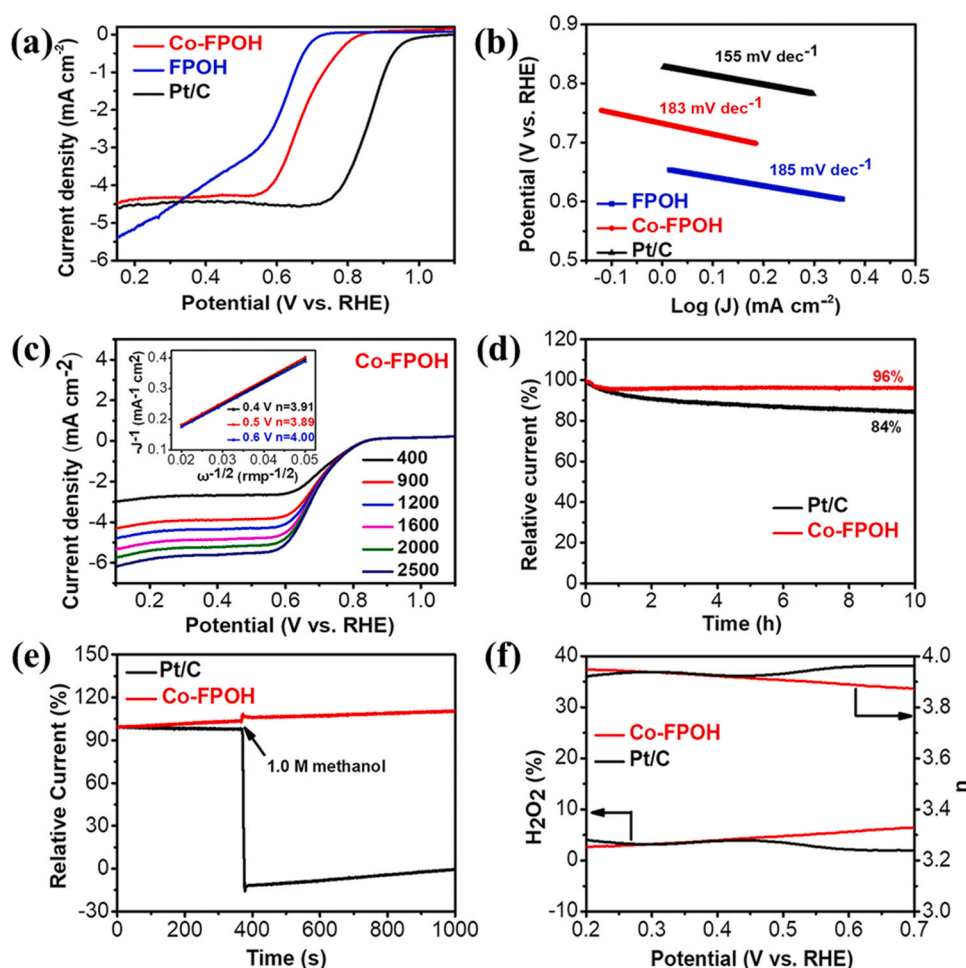


**Fig. 5.** (a) LSV curves and (b) Tafel plots of Co-FPOH, FPOH and commercial Pt/C (20%); (c) LSV curves of Co-FPOH measured at different rotational speeds (400, 900, 1200, 1600, 2000, and 2500 rpm) at 10 mV s<sup>-1</sup> in 0.1 M KOH saturated with O<sub>2</sub>, where the inset shows the corresponding K-L plots; (d) Chronoamperometric response of Co-FPOH and commercial Pt/C (20%) in O<sub>2</sub> saturated 0.1 M KOH solution under stirring for 10 h; (e) The durability test of Co-FPOH and 20 wt% Pt/C for methanol, where the arrow indicates the introduction of 2.033 mL (1.0 M) methanol; (f) H<sub>2</sub>O<sub>2</sub> yields of Co-FPOH and commercial Pt/C (20%) at varied potentials and the corresponding electron transfer numbers (n).

about the ORR electrocatalytic reaction mechanism can be obtained from the Tafel slope plot, which is determined by the mass transport in the mixed kinetic diffusion control zone [67]. As presented in Fig. 5b, the Co-FPOH shows a lower Tafel slope of 183 mV dec<sup>-1</sup> than FPOH (185 mV dec<sup>-1</sup>), demonstrating superior ORR dynamics.

The electrocatalytic kinetics of Co-FPOH was further examined by RDE tests at different rotating speeds (Fig. 5c). The linearly fitted K-L plots of the inset of Fig. 5c demonstrate the *n* value is ~4e<sup>-</sup> during ORR catalytic reaction, which is close to the theoretical value of Pt/C (*n* = 4.00), demonstrating the four-electron ORR process [68]. The Chronoamperometric response (*i*-*t*) of Co-FPOH and Pt/C electrocatalyst are demonstrated in Fig. 5d. It can be clearly realized that Co-FPOH shows excellent cycle stability with a current retention of 96% after the test of 10 h, superior to that of Pt/C (84%). The excellent long-term stability is mainly due to the changeability of local electric distribution of Co-FPOH to prevent the expire of the electrocatalyst active site. The methanol tolerance of Co-FPOH and Pt/C can be seen from Fig. 5e. When 2.033 mL (1.0 M) methanol is added, the relative current of Co-FPOH does not change significantly, indicating its very outstanding methanol tolerance. As shown in Fig. 5f, the hydrogen peroxide yields of Co-FPOH and Pt/C are both less than 10%, and their *n* value at different potentials is close to 4, which is consistent with the above *n* calculated by K-L equation.

### 3.4. Rechargeable zinc-air batteries

Due to the outstanding ORR/OER electrocatalytic activity of Co-FPOH, we used it as an air cathode to assemble a ZAB to estimate its practical application [59]. Fig. 6a and Fig. S6 demonstrate the

construction of the assembled ZAB, using a polished zinc as the anode, Co-FPOH loaded on carbon paper as the air cathode and a solution of KOH and Zn(Ac)<sub>2</sub> as the electrolyte. To illustrate the excellent performance of Co-FPOH electrocatalyst, the precious metal Pt/C@RuO<sub>2</sub> (weight ratio = 1:1) as an air cathode was tested as well. As shown in Fig. 6b and Fig. S7, the Co-FPOH based battery shows a higher open circuit voltage of 1.42 V compared with Pt/C@RuO<sub>2</sub> based battery (1.39 V). The specific capacity of Co-FPOH catalyst calculated by the mass of zinc consumed measured at 10 mA cm<sup>-2</sup> was 817 mAh g<sub>Zn</sub><sup>-1</sup>, higher than that of Pt/C@RuO<sub>2</sub> of 800 mAh g<sub>Zn</sub><sup>-1</sup> (Fig. 6c). And the specific capacity of Co-FPOH is evidently superior to those of previously reported catalysts (Table S4). The results firmly demonstrate that the Co-FPOH is very ideal for ZABs.

Discharge polarization curves and power density curves were obtained for ZABs with Co-FPOH are displayed in Fig. 6d. Obviously, the ZAB with Co-FPOH exhibits a peak power density (167.8 mW cm<sup>-2</sup>), which is larger than that of the ZAB with Pt/C@RuO<sub>2</sub> (77 mW cm<sup>-2</sup>) and also significantly superior to those of previously reported catalysts (Table S4). The discharging rate performance of the ZABs was then investigated at a gradually increased current density (e.g., 5, 10, 15 and 20 mA cm<sup>-2</sup>) and then at a gradually decreased current density (e.g., 20, 15, 10, 5 mA cm<sup>-2</sup>) for 14,000 s. As claimed in Fig. 6e, the battery with Co-FPOH delivers the voltage plateaus of 1.242, 1.210, 1.181, 1.156, 1.179, 1.210, and 1.244 V, while the battery with Pt/C@RuO<sub>2</sub> shows 1.232, 1.199, 1.172, 1.142, 1.177, 1.205, and 1.246 V, suggesting better rate performance.

As a description, two zinc-air batteries with Co-FPOH in series can readily light up a ~3 V red LED electronic display screen with high working stability (Fig. 6f). Fig. 6g demonstrates the long cycle stability

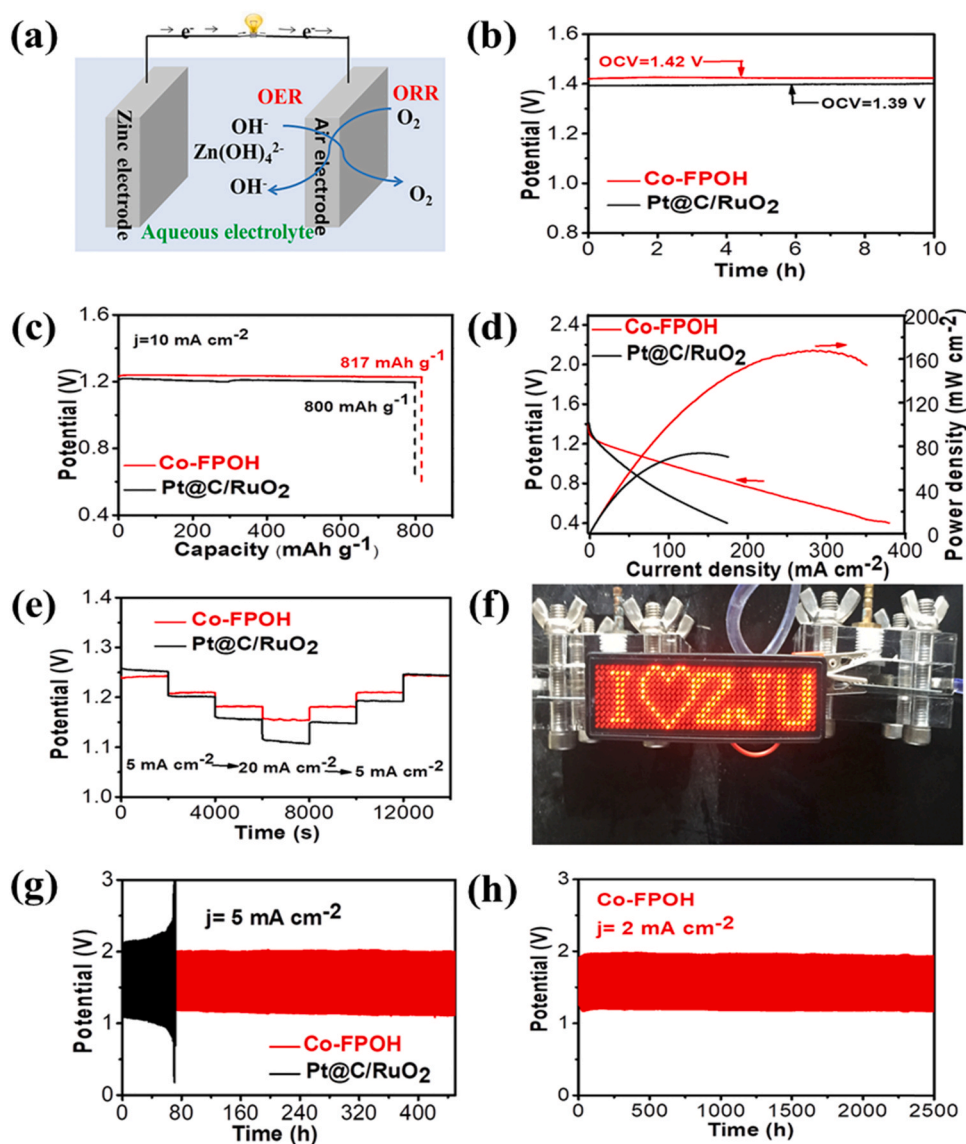


**Fig. 6.** (a) Scheme of a conventional ZAB; (b) Open circuit voltage measured with Co-FPOH and Pt/C/RuO<sub>2</sub> as the cathode of a zinc-air battery; (c) Discharge specific capacity of the battery assembled with Co-FPOH and Pt/C/RuO<sub>2</sub> at 10 mA cm<sup>-2</sup>; (d) Polarization and power density curves of the ZAB with Co-FPOH and Pt/C/RuO<sub>2</sub>; (e) Galvanostatic discharge voltage curves at varying current densities of 5, 10, 15 and 20 mA cm<sup>-2</sup>; (f) Photograph of a lighted light emitting diode (LED ~3 V) powered by zinc-air batteries (two) in series; (g) Galvanostatic discharge curves of ZAB with Co-FPOH and Pt/C/RuO<sub>2</sub> at a current density of 5 mA cm<sup>-2</sup>. (h) Galvanostatic discharge curves of ZABs with Co-FPOH at a current density of 2 mA cm<sup>-2</sup>.

of ZABs at 5 mA cm<sup>-2</sup>. The ZABs with Co-FPOH has a low charge potential (1.92 V) and high discharge potential (1.23 V), representing a small potential gap of 0.69 V. And the ZABs with Co-FPOH reveal a long-term cycle performance for 450 h at 5 mA cm<sup>-2</sup>, where the change of the potential gap is fairly small. In contrast, the potential gap exhibits a quick elevation for ZABs with Pt/C/RuO<sub>2</sub> as a cathode, which is believed to be the result of serious polarization. Especially, the long-term cycling measurement was carried out at a current density of 2 mA cm<sup>-2</sup>, as shown in Fig. 6h. The ZABs loaded with Co-FPOH can retain stable about 2500 h, and the potential gap is as small as 0.8 V. The above results firmly identify the outstanding electrochemical performance of the ZABs assembled in this work.

#### 4. Conclusions

In summary, we have adopted a novel water-oil two-phase hydrothermal method to synthesize micro-spherical cobalt-doped Fe<sub>5</sub>(PO<sub>4</sub>)<sub>4</sub>(OH)<sub>3</sub>·H<sub>2</sub>O. This synthesis method can control the progress of the reaction by controlling the diffusion rate of the material at the sub-interface formed by the water and oil phases to realize the special morphologies of nanostructures. The water-oil two-phase synthesis method with phytic acid as the water phase has guiding significance for

the synthesis of transition metal phosphates and hydrogen phosphates. After doping Co atoms into the matrix of FPOH, the electrocatalytic performances of OER and ORR are both significantly improved for the resulted Co-FPOH. The Co-FPOH has a fairly low oxygen evolution potential of about 1.52 V. The constructed ZAB with Co-FPOH attains a discharge specific capacity of 817 mAh g<sub>Zn</sub><sup>-1</sup> at a current density of 10 mA cm<sup>-2</sup>, a super high peak power density of 167.8 mW cm<sup>-2</sup>, and a super long-term cycling stability at a current density of 5 mA cm<sup>-2</sup> (450 h). The results presented in this work not only provide a new insight to the design of non-noble metal bifunctional electrocatalysts, but also facilitate the fabrication of advanced ZABs with long life and high power density for practical applications.

#### CRediT authorship contribution statement

L. T. Song, the first author for the paper and the leader of this work, making contribution to the most of jobs in the paper. T. L. Zheng, the co-first author for the paper, making contribution to lots of jobs in the paper. H. Q. Chen, and W. Z. Zheng, making contribution to the measurement of materials. J. L. Lian and Y. Wu, making contribution to the fabrication of ZABs. L. R. Zheng, Y. Hou, J. Chen, and Z. Z. Ye, making contribution to the discussion of the paper. B. Lu and Q. G. He,



making contribution to the analysis and design of this work. **J. G. Lu**, making contribution to the design of this work and the direction of the paper.

### Declaration of Competing Interest

The authors declare that they have no known competing financial interests or personal relationships that could have appeared to influence the work reported in this paper.

### Acknowledgment

This work was supported by the National Natural Science Foundation of China (No. U20A20209 and 21978260), Zhejiang Provincial Key Research and Development Program (2021C01030), Zhejiang Provincial Natural Science Foundation of China (LD19E020001), Open Project of Laboratory for Biomedical Engineering of Ministry of Education, Zhejiang University, and Leading Innovative and Entrepreneur Team Introduction Program of Zhejiang (2019R01006).

### Appendix A. Supporting information

Supplementary data associated with this article can be found in the online version at [doi:10.1016/j.apcatb.2021.120712](https://doi.org/10.1016/j.apcatb.2021.120712).

### References

- [1] S. Bahadori, R. Hart, Y. Hao, Synthesis of cobalt, palladium, and rhodium nanoparticles, *Tungsten* 2 (2020) 261–288, <https://doi.org/10.1007/s42864-020-00057-3>.
- [2] Y. Meng, J. Li, S. Zhao, C. Shi, X. Li, L. Zhang, P. Hou, C. Liu, H. Cheng, Fluorination-assisted preparation of self-supporting single-atom Fe-N-doped single-wall carbon nanotube film as bifunctional oxygen electrode for rechargeable Zn-air batteries, *Appl. Catal. B: Environ.* 294 (2021), 120239, <https://doi.org/10.1016/j.apcatb.2021.120239>.
- [3] X. Lang, Z. Hu, C. Wang, Bifunctional air electrodes for flexible rechargeable Zn-air batteries, *Chin. Chem. Lett.* 32 (2021) 999–1009, <https://doi.org/10.1016/j.ccl.2020.10.005>.
- [4] L. Wang, X. Shi, Y. Jia, H. Cheng, L. Wang, Q. Wang, Recent advances in bismuth vanadate-based photocatalysts for photoelectrochemical water splitting, *Chin. Chem. Lett.* 32 (2021) 1869–1878, <https://doi.org/10.1016/j.ccl.2020.11.065>.
- [5] H. Wang, J. Chen, Y. Lin, X. Wang, J. Li, Y. Li, L. Gao, L. Zhang, D. Chao, X. Xiao, J. Lee, Electronic modulation of non-van der Waals 2D electrocatalysts for efficient energy conversion, *Adv. Mater.* 33 (2021), 2008422, <https://doi.org/10.1002/adma.202008422>.
- [6] V. Jose, J. Nsanizimana, H. Hu, J. Choi, X. Wang, J. Lee, Highly efficient oxygen reduction reaction activity of N-doped carbon–cobalt boride heterointerfaces, *Adv. Energy Mater.* 11 (2021), 2100157, <https://doi.org/10.1002/aenm.202100157>.
- [7] H. Wang, J. Li, K. Li, Y. Lin, J. Chen, L. Gao, V. Nicolosi, X. Xiao, J. Lee, Transition metal nitrides for electrochemical energy applications, *Chem. Soc. Rev.* 50 (2021) 1354–1390, <https://doi.org/10.1039/d0cs00415d>.
- [8] P. Prabhhu, J. Lee, Metalloenes as functional materials in electrocatalysis, *Chem. Soc. Rev.* 50 (2021) 6700–6719, <https://doi.org/10.1039/d0cs01041c>.
- [9] Y. Tian, J. Lu, H. Tang, X. Wang, L. Zhang, P. Hu, L. Zhou, Y. Wang, Y. Guo, R. Khatoon, Q. Zhang, Q. He, Y. He, M. Qiu, Y. Hou, Z. Ye, An ultra-stable anode material for high/low-temperature workable super-fast charging sodium-ion batteries, *Chem. Eng. J.* 422 (2021), 130054, <https://doi.org/10.1016/j.cej.2021.130054>.
- [10] H. Tang, K. Xia, J. Lu, J. Fu, Z. Zhu, Y. Tian, Y. Wang, M. Liu, J. Chen, Z. Xu, Y. Guo, R. Khatoon, H. Chen, Z. Ye, NiTe<sub>2</sub>-based electrochemical capacitors with high-capacitance AC line filtering for regulating TENGs to steadily drive LEDs, *Nano Energy* 84 (2021), 105931, <https://doi.org/10.1016/j.nanoen.2021.105931>.
- [11] P. Li, Z. Jin, J. Yang, Y. Jin, D. Xiao, Highly active 3D-nanoarray-supported oxygen-evolving electrode generated from cobalt-phytate nanoplates, *Chem. Mater.* 28 (2015) 153–161, <https://doi.org/10.1021/acs.chemmater.5b03470>.
- [12] Q. Zhou, S. Hou, Y. Cheng, R. Sun, W. Shen, R. Tian, J. Yang, H. Pang, L. Xu, K. Huang, Y. Tang, Interfacial engineering Co and MnO within N,S co-doped carbon hierarchical branched superstructures toward high-efficiency electrocatalytic oxygen reduction for robust Zn-air batteries, *Appl. Catal. B: Environ.* 295 (2021), 120281, <https://doi.org/10.1016/j.apcatb.2021.120281>.
- [13] V. Jose, H. Hu, E. Edison, W. Manalastas, H. Ren, P. Kidkhunthod, S. Sreejith, A. Jayakumar, J. Nsanizimana, M. Srinivasan, J. Choi, J. Lee, Modulation of single atomic Co and Fe sites on hollow carbon nanospheres as oxygen electrodes for rechargeable Zn–air batteries, *Small Methods* 5 (2020), 202000751, <https://doi.org/10.1002/smt.202000751>.
- [14] H. Lei, Z. Wang, F. Yang, X. Huang, J. Liu, Y. Liang, J. Xie, M. Javed, X. Lu, S. Tan, W. Mai, NiFe nanoparticles embedded N-doped carbon nanotubes as high-efficient electrocatalysts for wearable solid-state Zn-air batteries, *Nano Energy* 68 (2020), 104293, <https://doi.org/10.1016/j.nanoen.2019.104293>.
- [15] T. Liu, J. Mou, Z. Wu, C. Lv, J. Huang, M. Liu, A facile and scalable strategy for fabrication of superior bifunctional freestanding air electrodes for flexible zinc–air batteries, *Adv. Funct. Mater.* 30 (2020), 2003407, <https://doi.org/10.1002/adfm.202003407>.
- [16] L. Yang, J. Shui, L. Du, Y. Shao, J. Liu, L. Dai, Z. Hu, Carbon-based metal-free ORR electrocatalysts for fuel cells: past, present, and future, *Adv. Mater.* 31 (2019), 1804799, <https://doi.org/10.1002/adma.201804799>.
- [17] J. Gu, S. Magagula, J. Zhao, Z. Chen, Boosting ORR/OER activity of graphdiyne by simple heteroatom doping, *Small Methods* 3 (2019), 1800550, <https://doi.org/10.1002/smt.201800550>.
- [18] G. Sievers, A. Jensen, J. Quinson, A. Zana, F. Bizzotto, M. Oezaslan, A. Dworzak, J. Kirkensgaard, T. Smitshuysen, S. Kadkhodazadeh, M. Juelsholt, K. Jensen, K. Anklam, H. Wan, J. Schafer, K. Cepe, M. Escibano, J. Rossmesl, A. Quade, V. Bruser, M. Arenz, Self-supported Pt-CoO networks combining high specific activity with high surface area for oxygen reduction, *Nat. Mater.* 20 (2021) 208–213, <https://doi.org/10.1038/s41563-020-0775-8>.
- [19] L. Yu, P. Somfai, Enantioselective synthesis of anti-3-alkenyl-2-amido-3-hydroxy esters: application to the total synthesis of (+)-alexine, *RSC Adv.* 9 (2019) 2799–2802, <https://doi.org/10.1039/c9ra00173e>.
- [20] H. Liu, J. Qin, T. Rockward, J. Wu, J. Li, G. Li, Q. Mao, Y. Lv, X. Wang, S. Zhang, W. Shi, G. Chen, Q. He, Y. Jiang, H. Yu, R. Borup, Y. Wang, Y. Song, Photo-driven growth of a monolayer of platinum spherical-nanocrowns uniformly coated on a membrane toward fuel cell applications, *J. Mater. Chem. A* 8 (2020) 23284–23292, <https://doi.org/10.1039/d0ta07189g>.
- [21] J. Wang, H. Kong, J. Zhang, Y. Hao, Z. Shao, F. Ciucci, Carbon-based electrocatalysts for sustainable energy applications, *Prog. Mater. Sci.* 116 (2021), 100717, <https://doi.org/10.1016/j.pmatsci.2020.100717>.
- [22] Y. Xiao, T. Hu, X. Zhao, F. Hu, H. Yang, C. Li, Thermo-selenizing to rationally tune surface composition and evolve structure of stainless steel to electrocatalytically boost oxygen evolution reaction, *Nano Energy* 75 (2020), 104949, <https://doi.org/10.1016/j.nanoen.2020.104949>.
- [23] Z. Zhu, H. Yin, Y. Wang, C. Chuang, L. Xing, M. Dong, Y. Lu, G. Garcia, Y. Zheng, S. Chen, Y. Dou, P. Liu, Q. Cheng, H. Zhao, Coexisting single-atomic Fe and Ni sites on hierarchically ordered porous carbon as a highly efficient ORR electrocatalyst, *Adv. Mater.* 32 (2020), 2004670, <https://doi.org/10.1002/adma.202004670>.
- [24] Y. Yuan, Y. Lu, B.-E. Jia, H. Tang, L. Chen, Y. Zeng, Y. Hou, Q. Zhang, Q. He, L. Jiao, J. Leng, Z. Ye, J. Lu, Integrated system of solar cells with hierarchical NiCo<sub>2</sub>O<sub>4</sub> battery-supercapacitor hybrid devices for self-driving light-emitting diodes, *Nano-Micro Lett.* 11 (2019) 42, <https://doi.org/10.1007/s40820-019-0274-0>.
- [25] G. Fu, X. Yan, Y. Chen, L. Xu, D. Sun, J. Lee, Y. Tang, Boosting bifunctional oxygen electrocatalysis with 3D graphene aerogel-supported Ni/MnO particles, *Adv. Mater.* 30 (2018), 1704609, <https://doi.org/10.1002/adma.201704609>.
- [26] H. Liu, Y. Wang, X. Lu, Y. Hu, G. Zhu, R. Chen, L. Ma, H. Zhu, Z. Tie, J. Liu, Z. Jin, The effects of Al substitution and partial dissolution on ultrathin NiFeAl ternary layered double hydroxide nanosheets for oxygen evolution reaction in alkaline solution, *Nano Energy* 35 (2017) 350–357, <https://doi.org/10.1016/j.nanoen.2017.04.011>.
- [27] P. Prabhhu, V. Jose, J. Lee, Design strategies for development of TMD-based heterostructures in electrochemical energy systems, *Matter* 2 (2020) 526–553, <https://doi.org/10.1016/j.matt.2020.01.001>.
- [28] X. Hu, Y. Chen, M. Zhang, G. Fu, D. Sun, J. Lee, Y. Tang, Alveolate porous carbon aerogels supported Co<sub>9</sub>S<sub>8</sub> derived from a novel hybrid hydrogel for bifunctional oxygen electrocatalysis, *Carbon* 144 (2019) 557–566, <https://doi.org/10.1016/j.carbon.2018.12.099>.
- [29] G. Fu, Y. Wang, Y. Tang, K. Zhou, J. Goodenough, J. Lee, Superior oxygen electrocatalysis on nickel indium thiospinels for rechargeable Zn–air batteries, *ACS Mater. Lett.* 1 (2019) 123–131, <https://doi.org/10.1021/acsmaterlett.9b00093>.
- [30] G. Fu, J. Wang, Y. Chen, Y. Liu, Y. Tang, J. Goodenough, J. Lee, Exploring indium-based ternary thiospinel as conceivable high-potential air-cathode for rechargeable Zn-air batteries, *Adv. Energy Mater.* 8 (2018), 1802263, <https://doi.org/10.1002/aenm.201802263>.
- [31] J. Zhang, X. Bai, T. Wang, W. Xiao, P. Xi, J. Wang, D. Gao, J. Wang, Bimetallic nickel cobalt sulfide as efficient electrocatalyst for Zn-air battery and water splitting, *Nano-Micro Lett.* 11 (2019) 2, <https://doi.org/10.1007/s40820-018-0232-2>.
- [32] C. Sha, B. Lu, H. Mao, J. Cheng, X. Pan, J. Lu, Z. Ye, 3D ternary nanocomposites of molybdenum disulfide/polyaniline/reduced graphene oxide aerogel for high performance supercapacitors, *Carbon* 99 (2016) 26–34, <https://doi.org/10.1016/j.carbon.2015.11.066>.
- [33] H. Chen, R. Liu, Y. Wu, J. Cao, J. Chen, Y. Hou, Y. Guo, R. Khatoon, L. Chen, Q. Zhang, Q. He, J. Lu, Interface coupling 2D/2D SnSe<sub>2</sub>/graphene heterostructure as long-cycle anode for all-climate lithium-ion battery, *Chem. Eng. J.* 407 (2021), 126973, <https://doi.org/10.1016/j.cej.2020.126973>.
- [34] J. Cao, K. Wang, J. Chen, C. Lei, B. Yang, Z. Li, L. Lei, Y. Hou, K. Ostrikov, Nitrogen-doped carbon-encased bimetallic selenide for high-performance water electrolysis, *Nano-Micro Lett.* 11 (2019) 67, <https://doi.org/10.1007/s40820-019-0299-4>.
- [35] H. Wang, Y. Wu, X. Yuan, G. Zeng, J. Zhou, X. Wang, J.W. Chew, Clay-inspired MXene-based electrochemical devices and photo-electrocatalyst: state-of-the-art progresses and challenges, *Adv. Mater.* 30 (2018), 1704561, <https://doi.org/10.1002/adma.201704561>.
- [36] J. Masa, I. Sinev, H. Mistry, E. Ventosa, M. Mata, J. Arbiol, M. Muhler, B. Roldan Cuenya, W. Schuhmann, Ultrathin high surface area nickel boride (Ni<sub>3</sub>B)

- nanosheets as highly efficient electrocatalyst for oxygen evolution, *Adv. Energy Mater.* 7 (2017), 1700381, <https://doi.org/10.1002/aenm.201700381>.
- [37] Y. Li, Z. Dong, L. Jiao, Multifunctional transition metal-based phosphides in energy-related electrocatalysis, *Adv. Energy Mater.* 10 (2019), 1902104, <https://doi.org/10.1002/aenm.201902104>.
- [38] J. Chen, C. Fan, X. Hu, C. Wang, Z. Huang, G. Fu, J.M. Lee, Y. Tang, Hierarchically porous Co/CoxMy (M = P, N) as an efficient Mott-Schottky electrocatalyst for oxygen evolution in rechargeable Zn-air batteries, *Small* 15 (2019), 1901518, <https://doi.org/10.1002/smll.201901518>.
- [39] M. Balogun, Y. Huang, W. Qiu, H. Yang, H. Ji, Y. Tong, Updates on the development of nanostructured transition metal nitrides for electrochemical energy storage and water splitting, *Mater. Today* 20 (2017) 425–451, <https://doi.org/10.1016/j.mattod.2017.03.019>.
- [40] H. Kim, J. Park, I. Park, K. Jin, S. Jerng, S.H. Kim, K. Nam, K. Kang, Coordination tuning of cobalt phosphates towards efficient water oxidation catalyst, *Nat. Commun.* 6 (2015) 8253, <https://doi.org/10.1038/ncomms925>.
- [41] Y. Zhou, H. Zeng, 3D networks of CoFePi with hierarchical porosity for effective OER electrocatalysis, *Small* 14 (2018), 1704403, <https://doi.org/10.1002/smll.201704403>.
- [42] S. Sheehan, J. Thomsen, U. Hintermair, R. Crabtree, G. Brudvig, C. Schmuttenmaer, A molecular catalyst for water oxidation that binds to metal oxide surfaces, *Nat. Commun.* 6 (2015) 6469, <https://doi.org/10.1038/ncomms7469>.
- [43] M. Pramanik, C. Li, M. Imura, V. Malgras, Y. Kang, Y. Yamauchi, Ordered mesoporous cobalt phosphate with crystallized walls toward highly active water oxidation electrocatalysts, *Small* 12 (2016) 1709–1715, <https://doi.org/10.1002/smll.201503187>.
- [44] C. Yang, C. Robert, D. Batuk, G. Cibir, A. Chadwick, V. Pimenta, W. Yin, L. Zhang, J. Tarascon, A. Grimaud, Phosphate ion functionalization of perovskite surfaces for enhanced oxygen evolution reaction, *J. Phys. Chem. Lett.* 8 (2017) 3466–3472, <https://doi.org/10.1021/acs.jpclett.7b01504>.
- [45] J. Wang, H. Zeng, CoHPi nanoflakes for enhanced oxygen evolution reaction, *ACS Appl. Mater. Interfaces* 10 (2018) 6288–6298, <https://doi.org/10.1021/acsami.7b17257>.
- [46] F. Massel, S. Ahmadi, M. Mahlin, Y. Liu, J. Guo, T. Edvinsson, H. Rensmo, L. Duda, Transition metal doping effects in Co-phosphate catalysts for water splitting studied with XAS, *J. Electron. Spectrosc. Relat. Phenom.* 224 (2018) 3–7, <https://doi.org/10.1016/j.elspec.2017.09.012>.
- [47] J. Zhang, Y. Yang, Z. Zhang, X. Xu, X. Wang, Rapid synthesis of mesoporous  $\text{NiCo}_3\text{--}x(\text{PO}_4)_2$  hollow shells showing enhanced electrocatalytic and supercapacitor performance, *J. Mater. Chem. A* 2 (2014) 20182–20188, <https://doi.org/10.1039/c4ta05278a>.
- [48] Y. Li, C. Zhao, Iron-doped nickel phosphate as synergistic electrocatalyst for water oxidation, *Chem. Mater.* 28 (2016) 5659–5666, <https://doi.org/10.1021/acs.chemmater.6b01522>.
- [49] S. Sultan, M. Ha, D. Kim, J. Tiwari, C. Myung, A. Meena, T. Shin, K. Chae, K. Kim, Superb water splitting activity of the electrocatalyst  $\text{Fe}_3\text{Co}(\text{PO}_4)_4$  designed with computation aid, *Nat. Commun.* 10 (2019) 5195, <https://doi.org/10.1038/s41467-019-13050-3>.
- [50] Z. Wang, M. Liu, J. Du, Y. Lin, S. Wei, X. Lu, J. Zhang, A facile co-precipitation synthesis of robust FeCo phosphate electrocatalysts for efficient oxygen evolution, *Electrochim. Acta* 264 (2018) 244–250, <https://doi.org/10.1016/j.electacta.2018.01.124>.
- [51] S. Ren, X. Duan, F. Ge, M. Zhang, H. Zheng, Trimetal-based N-doped carbon nanotubes arrays on Ni foams as self-supported electrodes for hydrogen/oxygen evolution reactions and water splitting, *J. Power Sources* 480 (2020), 228866, <https://doi.org/10.1016/j.jpowsour.2020.228866>.
- [52] N. Zhao, W. Nie, X. Liu, S. Tian, Y. Zhang, X. Ji, Shape- and size-controlled synthesis and dependent magnetic properties of nearly monodisperse  $\text{Mn}_3\text{O}_4$  nanocrystals, *Small* 4 (2008) 77–81, <https://doi.org/10.1002/smll.200700698>.
- [53] X. Guo, Q. Fan, L. Yu, J. Liang, W. Ji, L. Peng, X. Guo, W. Ding, Y. Chen, Sandwich-like  $\text{LiFePO}_4$ /graphene hybrid nanosheets: in situ catalytic graphitization and their high-rate performance for lithium ion batteries, *J. Mater. Chem. A* 1 (2013) 11534–11538, <https://doi.org/10.1039/c3ta12422c>.
- [54] J. Chen, Y. Song, D. Shan, E. Han, Modifications of the hydrotalcite film on AZ31 Mg alloy by phytic acid: The effects on morphology, composition and corrosion resistance, *Corros. Sci.* 74 (2013) 130–138, <https://doi.org/10.1016/j.corsci.2013.04.03>.
- [55] X. Chen, P. Li, Z. Jin, Y. Meng, H. Yuan, D. Xiao, Tri-metallic phytate in situ electrodeposited on 3D Ni foam as a highly efficient electrocatalyst for enhanced overall water splitting, *J. Mater. Chem. A* 5 (2017) 18786–18792, <https://doi.org/10.1039/c7ta05386j>.
- [56] F. Pan, X. Yang, D. Zhang, Chemical nature of phytic acid conversion coating on AZ61 magnesium alloy, *Appl. Surf. Sci.* 255 (2009) 8363–8371, <https://doi.org/10.1016/j.apsusc.2009.05.089>.
- [57] X. Gao, Y. Yu, Q. Liang, Y. Pang, L. Miao, X. Liu, Z. Kou, J. He, S. Pennycook, S. Mu, J. Wang, Surface nitridation of nickel-cobalt alloy nanocactoids raises the performance of water oxidation and splitting, *Appl. Catal. B: Environ.* 270 (2020), 118889, <https://doi.org/10.1016/j.apcatb.2020.118889>.
- [58] M. Xing, L. Kong, M. Liu, L. Liu, L. Kang, Y. Luo, Cobalt vanadate as highly active, stable, noble metal-free oxygen evolution electrocatalyst, *J. Mater. Chem. A* 2 (2014) 18435–18443, <https://doi.org/10.1039/c4ta03776f>.
- [59] D. Yin, Z. Jin, M. Liu, T. Gao, H. Yuan, D. Xiao, Microwave-assisted synthesis of the cobalt-iron phosphates nanosheets as an efficient electrocatalyst for water oxidation, *Electrochim. Acta* 260 (2018) 420–429, <https://doi.org/10.1016/j.electacta.2017.12.007>.
- [60] Y. Huang, S. Zhang, X. Lu, Z. Wu, D. Luan, X. Lou, Trimetallic spinel  $\text{NiCo}_2\text{--}x\text{Fe}_x\text{O}_4$  nanoboxes for highly efficient electrocatalytic oxygen evolution, *Angew. Chem. Int. Ed. Engl.* 60 (2021) 11841–11846, <https://doi.org/10.1002/anie.202103058>.
- [61] M. Wang, L. Árnadóttir, Z. Xu, Z. Feng, In situ X-ray absorption spectroscopy studies of nanoscale electrocatalysts, *Nano-Micro Lett.* 11 (2019) 47, <https://doi.org/10.1007/s40820-019-0277-x>.
- [62] X. Liu, L. Wang, P. Yu, C. Tian, F. Sun, J. Ma, W. Li, H. Fu, A stable Bifunctional catalyst for rechargeable zinc-air batteries: iron-cobalt nanoparticles embedded in a nitrogen-doped 3D carbon matrix, *Angew. Chem. Int. Ed. Engl.* 57 (2018) 16166–16170, <https://doi.org/10.1002/anie.201809009>.
- [63] X. Wang, D. Cullen, Y. Pan, S. Hwang, M. Wang, Z. Feng, J. Wang, M. Engelhard, H. Zhang, Y. He, Y. Shao, D. Su, K. More, J. Spendelow, G. Wu, Nitrogen-coordinated single cobalt atom catalysts for oxygen reduction in proton exchange membrane fuel cells, *Adv. Mater.* 30 (2018), 1706758, <https://doi.org/10.1002/adma.201706758>.
- [64] P. Yu, L. Wang, F. Sun, Y. Xie, X. Liu, J. Ma, X. Wang, C. Tian, J. Li, H. Fu, Co nanoislands rooted on Co-N-C nanosheets as efficient oxygen electrocatalyst for Zn-air batteries, *Adv. Mater.* 31 (2019), 1901666, <https://doi.org/10.1002/adma.201901666>.
- [65] T. Wang, Q. Zhou, X. Wang, J. Zheng, X. Li, MOF-derived surface modified Ni nanoparticles as an efficient catalyst for the hydrogen evolution reaction, *J. Mater. Chem. A* 3 (2015) 16435–16439, <https://doi.org/10.1039/c5ta04001a>.
- [66] Y. Niu, X. Teng, S. Gong, Z. Chen, A bimetallic alloy anchored on biomass-derived porous N-doped carbon fibers as a self-supporting bifunctional oxygen electrocatalyst for flexible Zn-air batteries, *J. Mater. Chem. A* 8 (2020) 13725–13734, <https://doi.org/10.1039/d0ta03288c>.
- [67] I. Amiin, X. Liu, Z. Pu, W. Li, Q. Li, J. Zhang, H. Tang, H. Zhang, S. Mu, From 3D ZIF nanocrystals to Co-Nx/C nanorod array electrocatalysts for ORR, OER, and Zn-air batteries, *Adv. Funct. Mater.* 28 (2018), 1704638, <https://doi.org/10.1002/adfm.201704638>.
- [68] M. Pegis, C. Wise, D. Martin, J. Mayer, Oxygen reduction by homogeneous molecular catalysts and electrocatalysts, *Chem. Rev.* 118 (2018) 2340–2391, <https://doi.org/10.1021/acs.chemrev.7b00542>.